Journal of Magnetism and Magnetic Materials 427 (2017) 300–305

Contents lists available at ScienceDirect

Journal of Magnetism and Magnetic Materials

journal homepage: www.elsevier.com/locate/jmmm

# Separation of magnetic beads in a hybrid continuous flow microfluidic device

Abhishek Samanta[a], Ranjan Ganguly[b], Amitava Datta[b], Nipu Modak[c,*]

[a] Haldia Institute of Technology, Production Engineering Department, Haldia, India
[b] Jadavpur University, Power Engineering Department, India
[c] Jadavpur University, Mechanical Engineering Department, India

ARTICLE INFO

*Keywords:*
Magnetophoresis
Immunomagnetic separation
Magnetic Microspheres
Microfluidics

ABSTRACT

Magnetic separation of biological entities in microfluidic environment is a key task for a large number of bio-analytical protocols. In magnetophoretic separation, biochemically functionalized magnetic beads are allowed to bind selectively to target analytes, which are then separated from the background stream using a suitably imposed magnetic field. Here we present a numerical study, characterizing the performance of a magneto-phoretic hybrid microfluidic device having two inlets and three outlets for immunomagnetic isolation of three different species from a continuous flow. The hybrid device works on the principle of split-flow thin (SPLITT) fractionation and field flow fractionation (FFF) mechanisms. Transport of the magnetic particles in the microchannel has been predicted following an Eulerian-Lagrangian model and using an in-house numerical code. Influence of the salient geometrical parameters on the performance of the separator is studied by characterizing the particle trajectories and their capture and separation indices. Finally, optimum channel geometry is identified that yields the maximum capture efficiency and separation index.

## 1. Introduction

Magnetic separation of immunochemically linked biological entities on functionalized magnetic beads offers a promising route for miniaturizing clinical diagnostic applications. Nonmagnetic moieties of a wide spectrum of biophysical and biochemical traits can be bound to micron-scale magnetic beads and can be separated by the application of externally applied magnetic field [1]. Immunomagnetic separation technique offers several advantages over other kinds of separation methods envisaged in microfluidic devices: it offers facile, non-contact maneuverability of the magnetic particles (conjugated with biomaterials) with the help of external magnetic field; magnetic bead-analyte conjugates have strong magnetic contrast in most of the biological media, facilitating magnetic transport and magnetic diagnosis; availability of magnetic particles over a wide range of particle size and the diversity of biofunctionalization offers easy choice of particles to suit a specific application. However, selective separation of magnetic microspheres (and the tagged biomaterials) in a microfluidic environment is a challenging task. For example, the simplest design of magnetic trap [2] cannot be used to separate beads of different magnetophoretic mobility. Magnetic Split flow thin fractionation (SPLITT) allows microfluidic separation of magnetic beads of different mobility into co-flowing streams separated by thin splitters at the outlets of the microchannel [3]. This is achieved by imposing a magnetic field gradient along the transverse direction of the polydispersed suspension flow through the microchannel. Field flow fractionation (FFF) is another kind of microfluidic separation method, developed by Giddings [4], which adopts a flow-based chromatography type fractionation technique. Microspheres of different mobility are separated, by using externally applied field in the transverse direction, into streams that branch out from the main microchannel at different axial locations along the flow. FFF offers the advantages of simultaneous separation and measurement, and hence, is useful in bio molecules and cell separation and diagnosis [5] and biosensors [6]. While FFF design is less compact, SPLITT designs are more vulnerable to cross-contamination. It is therefore essential to maintain the separation throughput and minimize the non-specific crossover in SPLITT device by appropriately designing the microchannel and the magnetic field. Hoyos et al. [7] created a localized magnetic field by applying Halbach array which offered improved magnetic selectivity for transverse separation inside the SPLITT channel. System throughput can also be tuned by changing the channel layout. Although, the literature is replete with studies on FFF and SPLITT devices, to our knowledge, there is no report on integrating features of both the designs to develop a hybrid separator.

* Corresponding author.
*E-mail address:* nmechju@gmail.com (N. Modak).

http://dx.doi.org/10.1016/j.jmmm.2016.10.143
Received 27 June 2016; Received in revised form 24 October 2016; Accepted 27 October 2016
Available online 01 November 2016
0304-8853/ 

Operating regimes of magnetophoretic FFF and SPLITT have been characterized earlier by this group, where the influence of salient design and operating parameters on the device performance have been analysed [3,8]. Both the types of designs were found to offer narrow operating windows for which the capture efficiency and separation indices were high. It is intuitive from these prior studies that operating the FFF or SPLITT devices with more than two particles is extremely sensitive to any variation of parameters.

For maximizing the efficiency of the microfluidic separation device, here we propose a hybrid device bearing the features of both an FFF and a SPLITT and analyze the separation performance. A homogeneous suspension (in a buffer liquid) of particles of three different magnetophoretic mobility is introduces into the channel through one inlet, while another inlet carries the buffer solution. The particles are separated through three different outlets. For separation of the particles, an appropriately designed magnetic field is imposed. The objective of this study is to prescribe the geometrical parameters such that the three types of particles get collected selectively at their designated outlet streams with minimum cross-contamination.

## 2. Theoretical formulations

Fig. 1 illustrates the schematic diagram of the hybrid separator that has a length $L$ and width $H$ through which a steady pressure-driven flow is analysed. The device comprises of two inlets ($Inlet_1$ and $Inlet_2$) and three outlets viz., $Outlet_1$, $Outlet_2$ and $Outlet_3$.

A homogeneous aqueous buffer suspension carrying three different particle types of equal number density is introduced through $inlet_1$ whereas $inlet_2$ allows only the aqueous buffer solution. For generating a magnetic field gradient in the channel a magnetic line dipole is positioned at a location ($X_{mag}$, $Y_{mag}$) (see Fig. 1) in such a manner that the magnetic particles experience a magnetophoretic movement in the transverse direction, eventually leading them through the outlets $Outlet_1$, $Outlet_2$ and $Outlet_3$.

With the proper geometrical orientation of the outlets, the particles with larger and smaller magnetophoretic mobility should escape through the outlet streams $Outlet_1$ and$Outlet_2$, respectively, while the nonmagnetic particle is expected to separate out through $Outlet_3$ (can be seen in Fig. 1). Particles moving with the carrier fluid inside the channel will experience a magnetic body force ($\mathbf{F}_m$), viscous drag force ($\mathbf{F}_d$) by the carrier fluid, the gravitational force ($\mathbf{F}_g = 4/3(\rho_p - \rho)\pi a^3 g$) and the thermal Brownian force, ($\mathbf{F}_b = R_d\sqrt{12\pi a\eta K_b T/dt}$, where $\mathbf{R_d}$ is a uniform random number vector whose value lies between 0 and 1, $K_b$ is the Boltzmann constant, $T$ is the absolute temperature and $dt$ is the time interval over which the Brownian force is resolved) [9].

The Lagrangian motion of a single particle, influenced by these forces can be expressed as

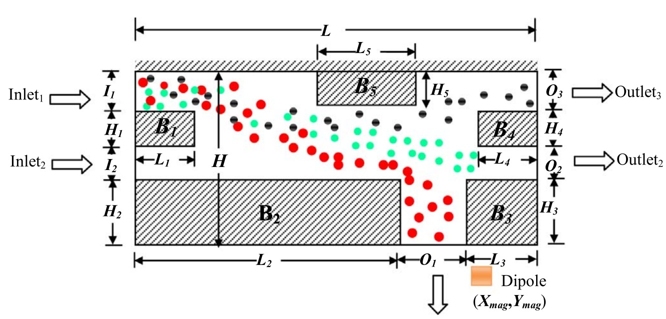


**Fig. 1.** Schematic of magnetophoretic hybrid device and the computational domain; the line dipole P is placed at ($X_{mag}$, $Y_{mag}$); red dots denote particles having larger magnetophoretic mobility than the cyan ones; black dots denote nonmagnetic particles; alteration in the flow passage is created by varying the dimensions of the rectangular blocks (solid walls) $B_1$, $B_2$, $B_3$, $B_4$ and $B_5$. (For interpretation of the references to color in this figure legend, the reader is referred to the web version of this article.)

$$\frac{4}{3}\pi a^3\rho_p\frac{dV_p}{dt}=[\mathbf{F}_g+\mathbf{F}_m+\mathbf{F}_d+\mathbf{F}_B] \tag{1}$$

Brownian force becomes negligible for particles exceeding 40 nm [10]; on the contrary, their size (~ 1 μm) and mass (~$7.5\times10^{-15}$ kg) renders the inertial and gravitational forces negligibly small. Therefore, the forces which can play major role in the present study are the magnetic and drag forces, which can be respectively expressed as [11]

$$\mathbf{F}_m=\frac{4}{3}\mu_0\pi a^3\chi_{eff}\frac{1}{2}\nabla(\mathbf{H}.\ \mathbf{H})\text{and}\mathbf{F}_d=6\pi a\eta K_{wall}(\mathbf{V}-\mathbf{V}_P). \tag{2}$$

The wall drag coefficients $K_{wall}^{\parallel}$ and $K_{wall}^{\perp}$ (for the drag forces in, respectively, the parallel and perpendicular directions to the wall) components can be expressed as $K_{wall}^{\parallel}=[1-9\xi/16]^{-1}$, and$K_{wall}^{\perp}=[1-9\xi/8]^{-1}$ where, ξ is the ratio of the particle diameter to its distance from the wall [12] and the effective magnetic susceptibility $\chi_{eff}$ [13] of the particle is

$$\chi_{eff} = \frac{\chi_i}{1+(\chi_i/3)} \tag{3}$$

Thus, reckoning the significant forces on a particle, Eq. (1) can be written as

$$\mathbf{V}_P=\mathbf{V}+\frac{1}{6\pi a\eta K_{wall}}\mathbf{F}_m \tag{4}$$

The instantaneous position of any particle can be calculated by integration of Eq. (4), once the initial position of the particle is specified.

Placed near $Outlet_1$ (as shown in Fig. 1), the line dipole has a strength $P$. In a practical MEMS device, such a line dipole may be produced by a pair of parallel conductors, carrying currents in opposite directions, and a soft magnetic core to buttress the field. The resulting magnetic field $\mathbf{H}$ at any location ($r$,$\phi$) from the virtual origin of the line dipole, can be expressed as [14]

$$\mathbf{H}=\frac{P}{r^2}(\hat{e}_r\sin\varphi-\hat{e}_\varphi\cos\varphi) \tag{5}$$

The drag force on the particles is influenced by the continuum phase (the host buffer liquid) velocity. The continuum phase follows the conservation of mass and momentum as specified by

$$\frac{\partial\rho}{\partial t}+\nabla.(\rho\mathbf{V})=0,\text{ and} \tag{6}$$

$$\frac{\partial}{\partial t}(\rho\mathbf{V})+\nabla.(\rho\mathbf{V}\mathbf{V})=-\nabla P+\nabla.\ \underline{\underline{\tau_v}}-\lambda\mathbf{F}_d, \tag{7}$$

where $\tau_v$ denotes the viscous stress, $\lambda$ the local particle density [15] and the last term in Eq. (7) signifies the reaction of $\mathbf{F}_d$ (i.e., the force applied on the particle by the liquid). On the walls of the channel and the guide block, no slip boundary condition is considered. At the two inlets $Inlet_1$ and $Inlet_2$, identical plug flow velocity profiles ($U_{av}$) are considered, while zero gauge pressure is specified at all the outlets.

## 3. Numerical simulations

An Eulerian-Lagrangian approach was considered for this work for the particle-laden flow through the microchannel. The coupled mass and momentum equations for the liquid phase were solved using SOLA – an explicit finite difference technique [16]. Under a steady flow, the fluid phase was first solved by the Eulerian approach. Particle tracking was then completed in a 'frozen' flow-field. The drag force by the liquid on the particle and its reaction i.e., force exerted by particle on liquid was calculated, and then again the fluid phase was solved by considering the revised body force in the momentum equation. Particle trajectories were then re-calculated in the revised flow-field, and these sequences were repeated until the largest deviation of the momentum source term within the domain between two consecutive steps of iteration fell below a pre-set convergence criterion. Details about the numerical scheme may be found elsewhere [11]. Following a grid

**Table 1**
Values of the fluid and particle parameters considered for the study.

| | Fluid and Particle Parameters | | | | | | | |
|---|---|---|---|---|---|---|---|---|
| | $a_1$ (μm) | $a_2$ (μm) | $a_3$ (μm) | $P$ (A-m) | $\eta$ (Pa-s) | $\chi_1$ | $\chi_2$ | $U_{av}$ (m/s) |
| Values | 2 | 1 | 0.5 | 1.7 | 0.001 | 0.1 | 0.1 | 0.016 |

independence study, a 150×90 mesh configuration was chosen for the present simulations. The numerical code was validated [11] by comparing the particle trajectories with those obtained through analytical solution by Nandy et al. [17]. Also, the simulations are validated with experimental results of particle capture efficiency in a simple "in-line trap" configuration of Modak et al. [18].

## 4. Results and discussions

### 4.1. Particle transport for the base case

Simulations are conducted for a given set of particle and flow parameters (see Table 1), while the salient device geometry is chosen as described in Table 2 (see also Fig. 1). Fig. 2 shows trajectories of 100 large (2 μm radius, denoted by red lines) magnetic particle clusters, 100 small (1 μm radius, denoted by cyan lines) magnetic particle clusters and 100 nonmagnetic (0.5 μm radius, denoted by black lines) particle clusters released from Inlet$_1$ (i.e. $0.0015 \le y \le 0.002$ m). Initially, at the entry region of the channel all three types of particle clusters primarily experience the fluid drag force, as the magnetic force is relatively weak there due to large distance from the dipole. As the particles are advected downstream nearer to the line dipole, magnetic particles experience stronger magnetic force in the transverse direction, and the particles begin to show deviation towards the dipole.

Larger magnetic particles exhibit higher magnetophoretic mobility than the smaller ones. On the contrary, the nonmagnetic particles experience only the drag force and therefore, they follow the streamlines. Because of the combined drag and magnetic force fields, the particles are fractionated at their designated outlets. It is evident from Fig. 2 that 4 large and 49 small clusters of magnetic particle are captured in the Outlet$_1$. Outlet$_2$ receives 42 small magnetic particle clusters along with 19 nonmagnetic ones. Outlet$_3$ receives 80 number no. of nonmagnetic particle clusters along with 9 clusters of small magnetic particles.

### 4.2. Capture efficiency and separation index

The intended performance of the device is to collect the maximum number of particle clusters in their designated outlets with very little intermingling; larger magnetic particle clusters should be collected at Outlet$_1$ and the smaller should collect at Outlet$_2$, while the nonmagnetic particles are designated to Outlet$_3$. Therefore, the device perfor-

**Table 2**
Geometrical parameters considered for the study.[a]

| Parameters | Base values (mm) | Range (mm) | Parameters | Base values (mm) | Range(mm) |
|---|---|---|---|---|---|
| $H_1$ | 0.25 | 0.25–0.5 | $L_1$ | 1.0 | Constant |
| $H_2$ | 0.75 | 0.75–0.5 | $L_2$ | 4.5 | 3.5–5.1 |
| $H_3$ | 0.75 | 0.75–0.5 | $L_3$ | 1.0 | 0.4–2.0 |
| $H_4$ | 0.25 | 0.25–0.5 | $L_4$ | 1.0 | Constant |
| $H_5$ | 0.45 | 0–0.45 | $L_5$ | 1.6 | Constant |

[a] $H_i$ and $L_i$ denote the height and length of different sections of the channel; $I_i$ and $O_i$ denote the inlet and outlet dimensions as indicated in Fig. 1. Overall device dimension: $L$=6 mm and $H$=2 mm; the line dipole P (Fig. 1) is placed at $X_{mag}$=5 mm and $Y_{mag}$=−0.7 mm.

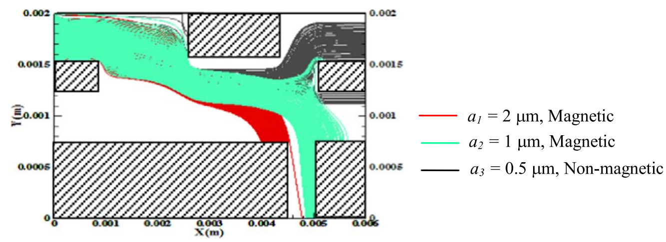


**Fig. 2.** Particle trajectories in the magnetophoretic hybrid device for the base case (Tables 1 and 2). (For interpretation of the references to color in this figure, the reader is referred to the web version of this article.).

mance is characterized here by capture efficiency (*CE*) i.e., the ratio of number of particle clusters (large magnetic, small magnetic and nonmagnetic) collected at their designated outlets (i.e., Outlet$_1$, Outlet$_2$ and Outlet$_3$, respectively) to the number of the corresponding particle clusters that has entered into the channel. Thus

$$CE_1 = \frac{\text{Number of large magnetic particle clusters captured at the Outlet}_1}{\text{Total number of the large magnetic particle clusters entered into the channel}}$$
$$CE_2 = \frac{\text{Number of small magnetic particle clusters captured at the Outlet}_2}{\text{Total number of the small magnetic particle clusters entered into the channel}}$$
$$CE_3 = \frac{\text{Number of nonmagnetic particle clusters captured at the Outlet}_3}{\text{Total number of the nonmagnetic particle clusters entered into the channel}} \quad (8)$$

Intermingling of different particles is practically unavoidable, leading to the possibility of collection of a few clusters of particles other than the designated ones at a particular outlet. Therefore, the performance of the device cannot be justified with *CE* alone. To quantify how good the purity of the separated streams is, separation index (*SI*) of the device is also evaluated as follows:

$$SI_1 = \frac{\text{Number of large magnetic particle clusters captured at outlet}_1}{\text{Total number of particle clusters captured at the outlet}_1}$$
$$SI_2 = \frac{\text{Number of small magnetic particle clusters captured at outlet}_2}{\text{Total number of particle clusters captured at the outlet}_2}$$
$$SI_3 = \frac{\text{Number of nonmagnetic particle clusters captured at outlet}_3}{\text{Total number of particle clusters captured at the outlet}_3} \quad (9)$$

As an extension to our previous work [3], here we intend to realise the effect of channel geometry on the capture efficiency (*CE*) and separation index (*SI*). In our previous study we have done wide parametric variations in terms of a group variable $\Pi$ (=$(a^2\chi P^2/\eta U_{av})$). Here we focus on the effect of variation of the key channel dimensions on the device performance, while all the parameters are kept at their base value (as listed in Table 1).

### 4.3. Effect of channel geometry

Fig. 1 shows the schematic diagram of the hybrid device with the channel dimensions. Layout of the flow passage can be altered by adjusting the relative locations and widths of the inlets and outlets. Our objective is to identify how these salient design parameters can influence *CE* and *SI* of the device. In our simulation, this variation is achieved by changing the transverse dimensions of the blocks B$_1$, B$_2$, B$_3$, B$_4$ and B$_5$, and the longitudinal dimensions of the blocks B$_2$ and B$_3$ (see Fig. 1). The total length ($L$) and width ($H$) of the separator chip and the dipole position ($X_{mag}$, $Y_{mag}$) are, however, kept fixed at their base values throughout the simulation. Fig. 3 describes the effect of flow passage area on the device performance. Starting from the base configuration (Table 2 and Fig. 2) the heights of blocks B$_2$ ($H_2$) and B$_3$ ($H_3$) are simultaneously decreased in steps of 500 μm and those of B$_1$ ($H_1$) and B$_4$ ($H_4$) are equally increased, keeping the widths of the inlet$_2$ ($I_2$) and outlet$_2$ ($O_2$) unchanged. This way, the flow passage is progressively dilated; at the same time the separation between the

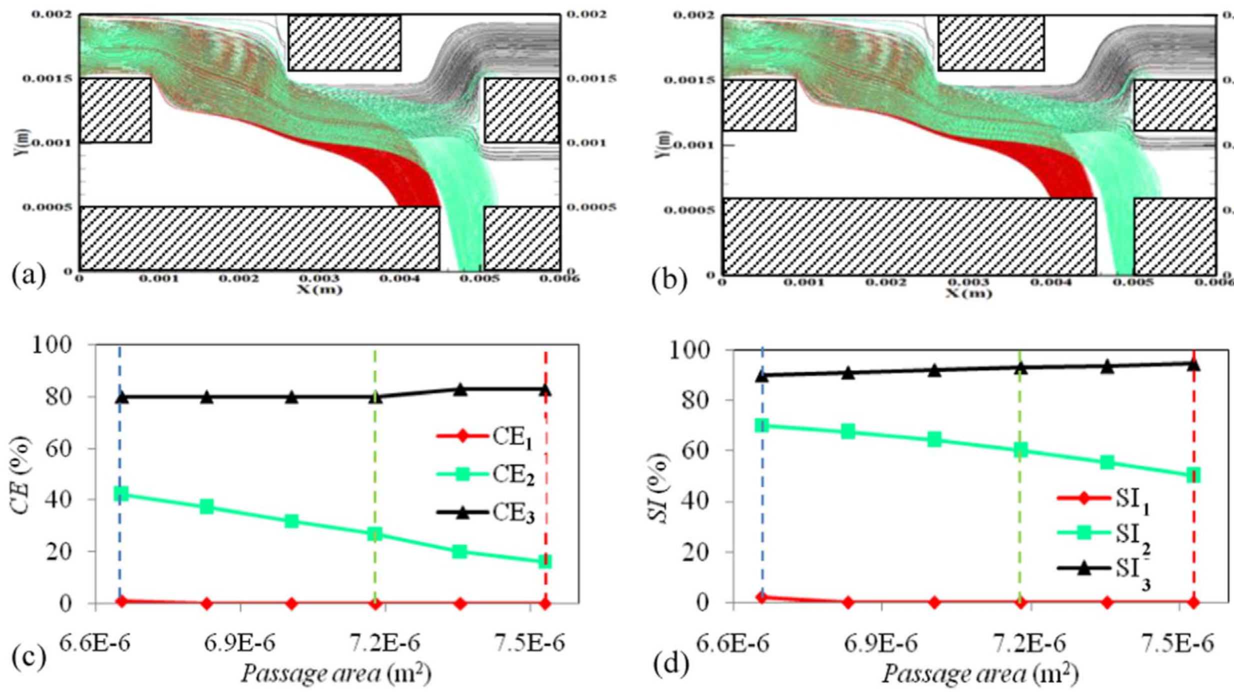


**Fig. 3.** Particle trajectories for (a) $H_1$=$H_4$=0.0005 m and $H_2$= $H_3$=0.0005 m, and (b) $H_1$=$H_4$=0.0004 m and $H_2$=$H_3$=0.0006 m. Variation of *CE* (c) and *SI* (d) with the passage area of the channel. Area of the passage is increased by simultaneously reducing the heights of blocks $B_2$ ($H_2$) and $B_3$ ($H_3$) in steps of 500 µm and increasing those of $B_1$ ($H_1$) and $B_4$ ($H_4$) equally. Vertical dotted lines denote the base case (blue), case-a (red) and case-b (green). (For interpretation of the references to color in this figure legend, the reader is referred to the web version of this article.)

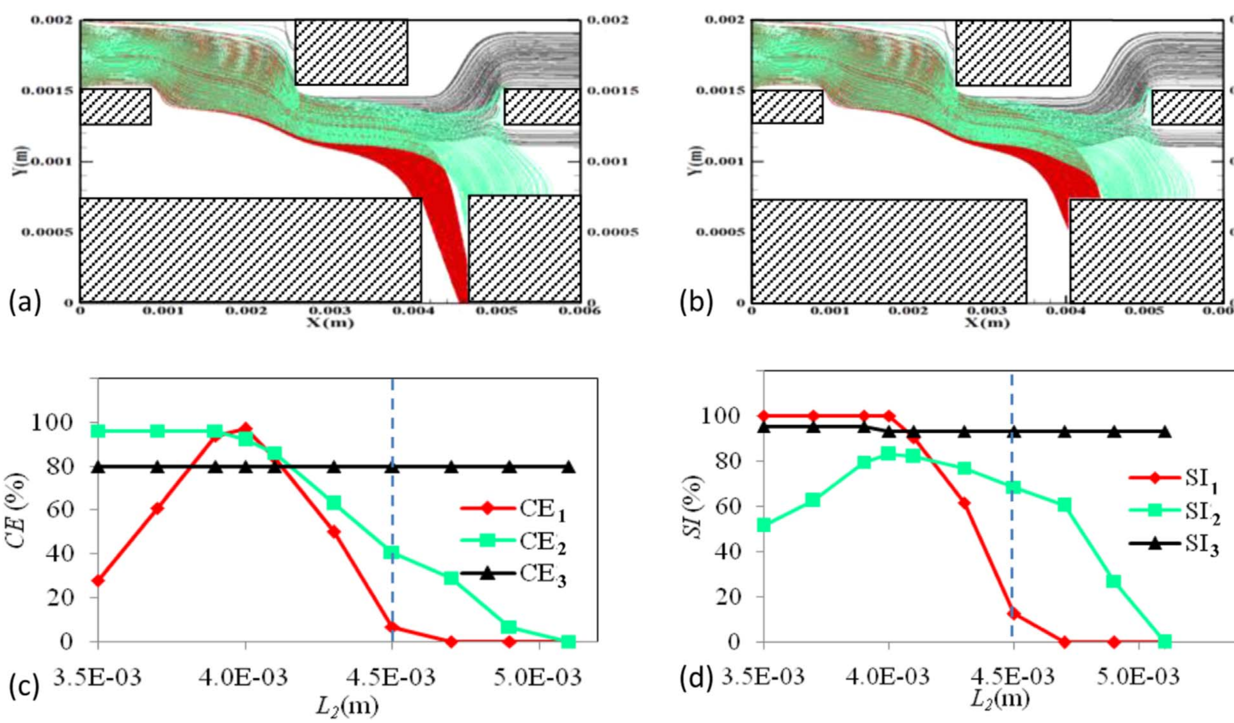


**Fig. 4.** Particle trajectories for (a) $L_2$=0.0041 m and (b) $L_2$=0.0035 m. Variation of *CE* (c) and *SI* (d) with the position of the $\text{Outlet}_1$ (shown in terms of $L_2$). Vertical dotted lines denote the base case.

dipole and the flow passage decreases. As can be seen from Figs. 2 and 3(a) and (b), nonmagnetic particle clusters, which experience only drag force (and therefore follow the streamlines emanating from $Inlet_1$), are directed through $O_3$. With increased $H_1$ and $H_4$ more number of streamlines from $\text{Inlet}_1$ passes through $\text{Outlet}_3$. As a result $CE_3$ increases slightly with the passage area (Fig. 3(c)). At the same time, due to decrease of $H_2$ and $H_3$ the lower bound of the flow passage is pushed down. This leads more number of small magnetic particles, which previously passed out through $\text{Outlet}_2$, to now escape through $\text{Outlet}_1$ (see Fig. 3(a) and (b)). This results in a reduction of $CE_2$ and $SI_2$ (Fig. 3(c) and (d)). Also, due to increased $H_4$, and reduction in $H_3$, trajectories of the large magnetic particles deviate downward, thereby trapping most of those particles on the wall of $B_2$. The base value of $O_1$ is so chosen that 4 clusters of large magnetic particles escape through

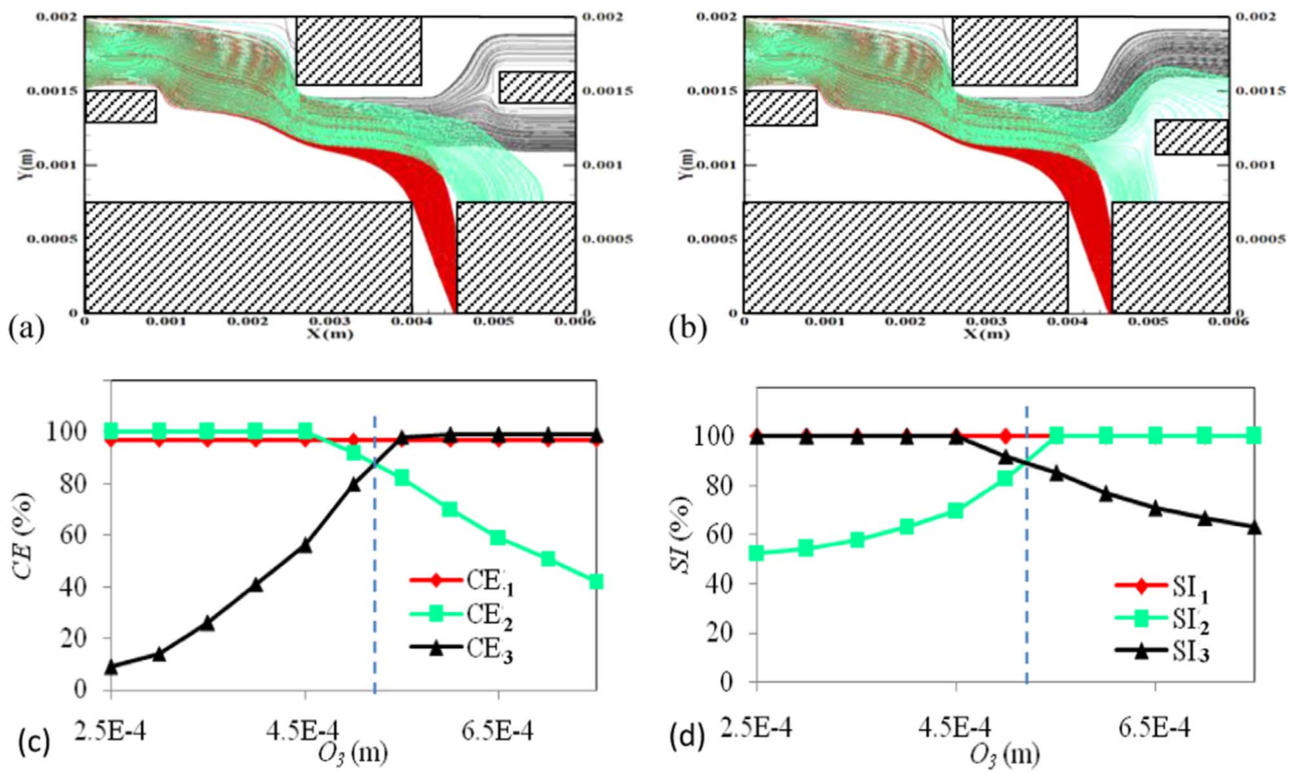


**Fig. 5.** Particle trajectories for (a) $O_3$=0.00035 m, $O_2$=0.00065 m and (b) $O_3$=0.0007 m, $O_2$=0.0003 m. $L_2$ (=0.004 m) and $L_3$ (=0.0015 m) are chosen from the optimum values observed in Fig. 4. Variation of *CE* (c) and *SI* (d) with the relative widths of $\text{Outlet}_2$ and $\text{Outlet}_3$ (shown in terms of $O_3$).

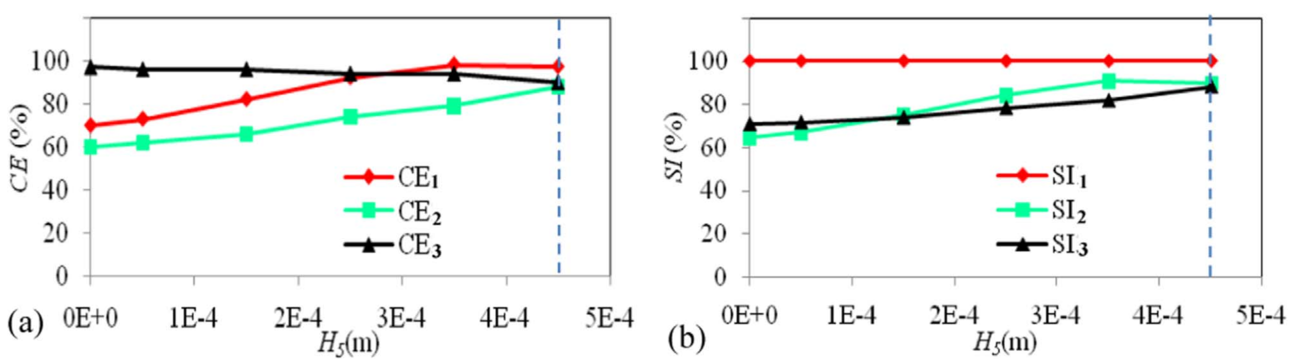


**Fig. 6.** Variation of *CE* (a) and *SI* (b) with $H_5$. Vertical dotted lines denote the best configuration for the range of study described in Table 2.

**Table 3**
Optimum values of the geometrical parameters.

| Parameters | Values (mm) | Parameters | Values (mm) | Parameters | Values (mm) |
|---|---|---|---|---|---|
| $H_1$ | 0.25 | $L_1$ | 1.0 | $I_1$ | 0.5 |
| $H_2$ | 0.75 | $L_2$ | 4.0 | $I_2$ | 0.5 |
| $H_3$ | 0.75 | $L_3$ | 1.5 | $O_1$ | 0.5 |
| $H_4$ | 0.25 | $L_4$ | 1.0 | $O_2$ | 0.52 |
| $H_5$ | 0.45 | $L_5$ | 1.6 | $O_3$ | 0.48 |

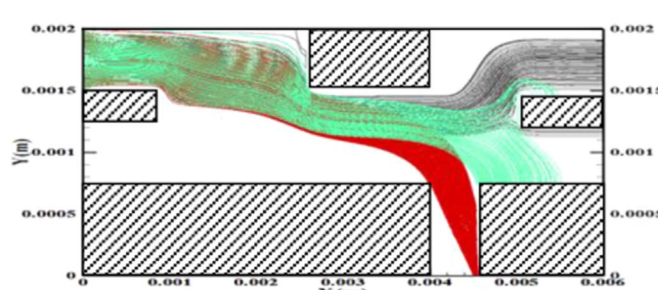


**Fig. 7.** Particle trajectory at optimized channel geometry.

$\text{Outlet}_1$. Lowering the values of $H_2$ and $H_3$ further aggravates the situation. The values of $CE_1$ and $SI_1$ decrease to zero beyond a flow passage area of $6.83\times10^{-6}$ m$^2$.

Fig. 4 shows the variation of *CE* and *SI* due to the change of the position of $\text{Outlet}_1$. This is achieved by simultaneously increasing $L_2$ and decreasing $L_3$, or vice versa, by equal magnitude, so that $O_1$ remains constant. Fig. 4(a) and (b) shows the particle trajectories for $L_2$ =0.0041 m and 0.0035 m, respectively. When $L_2$ is decreased from its base value of 0.0045–0.0041 m (accordingly, $L_3$ is increased from 0.001 to 0.0014 m), the $\text{Outlet}_1$ is shifted upstream by 400 µm. Under this condition, most of the large magnetic particles are found (Fig. 4(a)) to collect at the $\text{Outlet}_1$, yielding a large $CE_1$ (~84%) and $SI_1$ (90%). At the same time, with decreased $L_2$ more of the smaller magnetic particles, which were transported to the $\text{Outlet}_1$ in Fig. 2, now collect at the $\text{Outlet}_2$. This leads to an increased $CE_2$ over the base case. When $L_2$ is decreased further to 0.0035 m (see Fig. 4(b)), some of the large particles skip the $\text{Outlet}_1$ and collect at $\text{Outlet}_2$. This reduces both $CE_1$ and $SI_2$ as compared to the case of Fig. 4(a). The trajectories of nonmagnetic particles in Fig. 4(a) and (b), and their corresponding $CE$ and $SI$ values do not alter much from the base case. Fig. 4(c) and (d) graphically show the influence of $L_2$ on $CE$ and $SI$, where a peak of $CE_1$ at $L_2$=0.004 m is observed yielding $CE_1$=97% and $SI_1$=100%. On either sides of $L_2$=0.004 m $CE_1$ decreases; while $SI_1$ remains close to 100% for smaller value of $L_2$ and decreases sharply for $L_2 > 0.004$ m. Fig. 4(b) also shows that $CE_2$ remains high (~100%) for $L_2 < 0.004$ m and decreases monotonically at higher $L_2$. $CE_3$ and $SI_3$ are found almost constant – with increase or decrease of position of $\text{Outlet}_1$ there is no effect on $CE_3$ and $SI_3$ because nonmagnetic particles only follow streamlines from $I_1$. In the subsequent section of the paper, we choose $L_2$=0.004 m, since it simultaneously offers high values of $CE$ and $SI$ for all the three types of particles.

Once the optimum position of the $\text{Outlet}_1$ is found, we next evaluate the influence of the relative widths of the other two outlets on the performance of the separator. Fig. 5 shows how $CE$ and $SI$ vary with the outlet widths $O_2$ and $O_3$ while their combined width remains constant – thus an increase in $O_2$ (with respect to the base case) is accompanied by an equal decrease in $O_3$. $L_2$ and $L_3$ are chosen at their optimized values of 0.004 m, and 0.0015 m, while all other dimensions remain as per Table 2. Fig. 5(a) and (b) show the particle trajectories for $O_3$ =350 and 700 μm, respectively (base value of $O_3$ is 500 μm). The corresponding trends of $CE$ and $SI$ are plotted in Fig. 5(c) and (d). Comparing the trajectories of Fig. 5(a) and (b) with Fig. 2, it is apparent that the particle separation between the $\text{Outlet}_2$ and $\text{Outlet}_3$ is largely influenced by the flow fractionation. With increased $O_3$, more of the nonmagnetic particles try to escape through $\text{Outlet}_3$; $CE_3$ gradually increases and eventually saturates at 100% (Fig. 5(c)). However, with increased $O_3$ (and accompanying reduction of $O_2$) more clusters of the smaller magnetic particles also tend to flow out through it. This leads to a reduction in $CE_2$ and $SI_3$. Similarly, for low value of $O_3$, more clusters of nonmagnetic particles are collected through $\text{Outlet}_2$, resulting in a reduction in $CE_3$ and $SI_2$. These relative widths of $\text{Outlet}_2$ and $\text{Outlet}_3$ do not seem to affect trajectories of the large magnetic particles. As a result $CE_1$ and $SI_1$ remain constant, close to their optimized values observed from Fig. 4. From the plots of Fig. 5(c) and (d), we choose $O_3$ =520 μm and $O_2$ =480 μm as the best performance point (marked by the blue vertical dotted lines in the figures).

Finally, the influence of the width of the block $B_5$ is evaluated with the other geometries corresponding to the optimum condition observed in Fig. 5(c) and (d) marked by blue dotted lines. Fig. 6 shows the variation of $CE$ and $SI$ with variation of $H_5$. Figure 6(a) shows that both $CE_1$ and $CE_2$ increase with $H_5$. As the height of the block $B_5$ increases, both types of magnetic particles (large and small) are diverted closer to the dipole. This increases the average magnetic force on them, enhancing the particle capture. The optimized channel geometry in Fig. 5 is obtained for $H_5$=450 μm, for which the largest values of $CE$ and $SI$ are also observed in Fig. 6. The plots also show a nearly invariant $CE_3$ in Fig. 6 – nonmagnetic particles are not affected by magnetic field, therefore, bringing them closer to the magnetic field (by increasing $H_5$) does not eventually alter their capture efficiency. The $SI_1$ remains saturated at ~100% throughout the range of $H_5$, indicating no trace of the smaller particles in $\text{Outlet}_1$. For the conditions investigated in Fig. 6, the optimum value of $H_5$ is found to be 450 μm.

Table 3 summarizes the optimized geometry for the hybrid separator while the particle trajectory for the optimized channel geometry is shown in Fig. 7. The optimum configuration yields $CE_1$=97%, $SI_1$=100%, $CE_2$=88%, $SI_2$=90%, $CE_3$=90%, $SI_3$=88%. These are significantly higher than the previously reported capture efficiencies in FFF [8] and SPLITT [3] configurations. It is important to note that this optimized device performance is achieved with a lower dipole strength ($P$=1.7 A m) as compared to the previously used dipole strength ($P$=4 A m) [3]. Thus, the hybrid separator clearly offers a better collection and separation performance, and at the same time offers separation of three different types of particles.

## 5. Conclusions

The numerical study identifies the optimum channel geometry for optimized performance of magnetophoretic hybrid device to separate biological entities on a microfluidic platform practically for BioMEMS applications. Both $CE$ and $SI$ of the device are found to be strongly affected by the channel geometry. The effect of each salient geometrical parameters of the separator on $CE$ and $SI$ offers the design bases for the best device performance [3]. For the optimized channel geometry reported here, higher $CE$ and $SI$ values are obtained even with relatively lower dipole strength than those observed in our previously reported studies on FFF and SPLITT configurations. The proposed hybrid magnetic separator, therefore, offers an improved design for immunomagnetic separation for biomedical applications.

## References


[1] I.K. Puri, R. Ganguly, Particle transport in therapeutic magnetic fields, Annu. Rev. Fluid Mech. 46 (2014) 407–440. http://dx.doi.org/10.1146/annurev-fluid-010313-141413.

[2] A. Sinha, R. Ganguly, I.K. Puri, Numerical investigation of flow-through immunoassay in a microchannel, J. Appl. Phys. 107 (2010) 034907. http://dx.doi.org/10.1063/1.3284077.

[3] A. Samanta, N. Modak, A. Datta, R. Ganguly, Operating regimes of a magnetic split-flow thin (SPLITT) fractionation microfluidic device for immunomagnetic separation, Microfluid. Nanofluid 20 (2016) 87. http://dx.doi.org/10.1007/s10404-016-1751-0.

[4] J.C. Giddings, Field-flow fractionation: analysis of macromolecular, colloidal, and particulate materials, Science 260 (1993) 1456–1465. http://dx.doi.org/10.1126/science.8502990.

[5] K.E. McCloskey, J.J. Chalmers, M. Zborowski, Magnetic cell separation: characterization of magnetophoretic mobility, Anal. Chem. 75 (2003) 6668–6874. http://dx.doi.org/10.1021/ac034315j.

[6] D.L. Graham, H.A. Ferreira, P.P. Freitas, Magneto resistive based biosensors and biochips, Trends Biotechnol. 22 (2004) 455–462. http://dx.doi.org/10.1016/j.tibtech.2004.06.006.

[7] M. Hoyos, L. Moore, P.S. Williams, M. Zborowski, The use of a linear Halbach array combined with a step-SPLITT channel for continuous sorting of magnetic species, J. Magn. Magn. Mater. 323 (2011) 1384–1388. http://dx.doi.org/10.1016/j.jmmm.2010.11.051.

[8] N. Modak, A.R. Pal, A. Datta, R. Ganguly, Bioseparation in a microfluidic channel using magnetic field flow fractionation, Int. J. Micro Nanoscale Transp. 3 (2012) 21–34. http://dx.doi.org/10.1260/1759-3093.3.1-2.21.

[9] R. Ganguly, I.K. Puri, Field-assisted self assembly of superparamagnetic nanoparticles for bio-medical, MEMS and bioMEMS applications, Adv. Appl. Mech. 41 (2007) 293–335. http://dx.doi.org/10.1016/S0065-2156(07)41004-3.

[10] E.P. Furlani, Y. Sahoo, Analytical model for the magnetic field and force in a magnetophoretic microsystem, J. Phys. D: Appl. Phys. 39 (2006) 1724–1732. http://dx.doi.org/10.1088/0022-3727/39/9/003.

[11] N. Modak, A. Datta, R. Ganguly, Cell separation in a microfluidic channel using magnetic microspheres, Microfluid. Nanofluid 6 (2009) 647–660. http://dx.doi.org/10.1007/s10404-008-0343-z.

[12] R. Clift, J.R. Grace, M.E. Weber, Bubbles Drops and Particles, Academic Press, New York, 1978.

[13] K. Smistrup, O. Hansen, H. Bruus, M.F. Hansen, Magnetic separation in microfluidic systems using microfabricated electromagnets—experiments and simulations, J. Magn. Magn. Mater. 293 (2005) 597–604. http://dx.doi.org/10.1016/j.jmmm.2005.01.079.

[14] R. Ganguly, S. Sen, I.K. Puri, Heat transfer augmentation in a channel with a magnetic fluid under the influence of a linedipole, J. Magn. Magn. Mater. 271 (2004) 63–73. http://dx.doi.org/10.1016/j.jmmm.2003.09.015.

[15] G.M. Faeth, Evaporation and combustion of sprays, Prog. Energy Combust. Sci. 9 (1983) 1–76. http://dx.doi.org/10.1016/0360-1285(83)90005-9.

[16] C.W. Hirt, B.D. Nicols, N.C. Romero, Los Alamos Scientific Laboratory Report LA-5852, Los Alamos New Mexico, 1975.

[17] K. Nandy, S. Chaudhuri, R. Ganguly, I.K. Puri, Analytical model for the magnetophoretic capture of magnetic microspheres in microfluidic devices, J. Magn. Magn. Mater. 320 (2008) 1398–1405. http://dx.doi.org/10.1016/j.jmmm.2007.11.024.

[18] N. Modak, D. Kejriwal, K. Nandy, A. Datta, R. Ganguly, Experimental and numerical characterization of magnetophoretic separation for MEMS-based biosensor applications, Biomed. Microdev. 12 (2010) 23–34. http://dx.doi.org/10.1007/s10544-009-9354-0.